1 **Photocatalytic Oxidation of Dissolved Mn^{2+} by TiO₂ and the Formation of Tunnel**

2 **Structured Manganese Oxides**

3

4 Haesung Jung[1, 2], Colin Snyder[1], Wenqian Xu[3], Ke Wen[4], Mengqiang Zhu[4], Yan Li[5], Anhuai

5 Lu[5], Yuanzhi Tang[1]*

6

7 [1]School of Earth and Atmospheric Sciences, Georgia Institute of Technology, Atlanta, Georgia,

8 30332-0340, United States

9 [2]School of Civil, Environmental and Chemical Engineering, Changwon National University,

10 Changwon, Gyeongsangnam-do, 51140, Republic of Korea

11 [3]X-ray Science Division, Advanced Photon Source, Argonne National Laboratory, Lemont,

12 Illinois 60439, United States

13 [4]Department of Ecosystem Science and Management, University of Wyoming, Laramie,

14 Wyoming, 82071, United States

15 [5]Beijing Key Laboratory of Mineral Environmental Function, School of Earth and Space

16 Sciences, Peking University, Beijing, China

17

18 *Corresponding author.

19 Yuanzhi Tang: E-mail: yuanzhi.tang@eas.gatech.edu; Phone: (1) 404-894-3814

20   **ABSTRACT**

21   The redox reaction of manganese (Mn) is of great environmental, geological, and public

22   health significance, as Mn oxides control the distribution and electron flow of numerous nutrients

23   and contaminants in natural and engineered environments. Current understanding on the oxidation

24   pathways of Mn(II) to Mn(III/IV) mainly focuses on biotic processes due to their much higher

25   oxidation rates than those associated with abiotic processes. This study demonstrates rapid

26   photocatalytic oxidation of Mn^{2+}(aq) under circumneutral conditions catalyzed by naturally

27   abundant semiconducting TiO_2 minerals. Notably, the photocatalytic oxidation rates are

28   comparable to or even higher than those of reported biotic/abiotic processes. In addition, the rapid

29   photocatalytic oxidation leads to the formation of large tunnel structured Mn oxides (todorokite

30   and romanechite) on the surface of TiO_2. These findings suggest that photocatalytic oxidation of

31   Mn^{2+}(aq) by natural semiconducting minerals is likely an important yet previously overlooked

32   pathway for understanding the occurrence of natural Mn oxide coatings on rock surfaces. In

33   addition, considering the increasing input of photo-reactive engineered nanoparticles into

34   environmental systems, this study shows the potential impacts of nanoparticles on influencing

35   natural redox cycles.

36

37   **Keywords:** Mn oxides, Ti oxide, nanoparticles, photochemistry, oxidation

1. INTRODUCTION

Mn(III/IV) (oxyhydr)oxides (hereafter Mn oxides) are a group of ubiquitous natural minerals in terrestrial and aquatic settings. They play important roles in numerous elemental cycles and affect the electron flow in nature.[1-9] They have high reduction potential ($E_{\mathrm{MnO_2}/Mn^{2+}} = $ ~500 mV at pH 7)[10] and high specific surface area (around 10 to 200 m^2/g)[11, 12] and are among the most reactive minerals and the most significant solid oxidants in nature. Thus, understanding the redox reactions of Mn in fresh water and high salinity aqueous systems (e.g., sea water) has been considered a key to elucidate the geochemical electron cycles in the history of Earth and Mars.[13-16] With their strong redox reactivity and high adsorption capacity, Mn oxides and related compounds are also widely used in energy and environmental engineering systems for energy storage, water treatment, and contaminant removal.[17-21] For example, recent studies demonstrated the application of Mn oxides for harvesting energy from wastewater and salinity gradient[22, 23] as well as for the degradation of antimicrobial agents, organic contaminants, and heavy metals[23-28].

Because of the important roles that Mn oxides play in natural and engineered systems, many studies have explored the kinetics and mechanisms for their formation and transformation, as well as redox reactions involving Mn oxides. Previous studies showed that the abiotic homogeneous oxidation of Mn^{2+}(aq) by molecular oxygen is kinetically sluggish and takes years even though it is thermodynamically favorable.[29, 30] Mineral surface catalyzed heterogeneous oxidation of Mn^{2+}(aq) by molecular oxygen takes 5–2,800 days (half-life) under circumneutral conditions.[29, 31] In contrast, microbially mediated processes via enzymes (e.g., multicopper oxidase) or reactive oxygen species (ROS, such as superoxide) show much faster oxidation (1–69 days half-life).[31-34] Because of the widespread presence of Mn-oxidizing microorganisms and the fast oxidation rate, biotic processes have been generally accepted as the most significant contributor to

61   the oxidation of Mn^{2+}(aq) and formation of Mn oxides in natural low temperature environments.

62   Interestingly, recent studies showed that photochemically generated superoxide by dissolved

63   organic matter or nitrate can also enable indirect photooxidation of Mn^{2+}(aq) (i.e., oxidation of

64   Mn^{2+}(aq) by photochemically generated oxygen-related species) at rates comparable to biotic

65   processes.[35-39] These exciting results shed lights on the potentially overlooked contribution of

66   photochemistry, an abiotic process, to the oxidation of Mn^{2+}(aq) and formation of Mn oxides.

67   Notably, previously known biotic/abiotic processes typically lead to the formation of

68   highly disordered and poorly crystalline layered Mn oxides (LMO) that are structurally similar to

69   vernadite (δ-MnO_2) or hexagonal birnessite. Although diverse tunnel structured Mn oxides (TMO)

70   occur ubiquitously in many environmental settings[40], the detailed mechanisms of their formation

71   have not been clearly resolved in laboratory studies under circumneutral conditions. Most studies

72   showed the transformation of LMO to TMO under pH or temperature conditions significantly

73   deviating from low temperature circumneutral conditions.[41-44] In our recent study under

74   circumneutral pH and ambient temperature condition, we demonstrated redox cycling driven

75   transformation of LMO to TMO.[45] However, although this study provided a new angle for

76   understanding the transformation of LMO to TMO under fluctuating natural conditions such as

77   those at oxic/anoxic interfaces, direct formation of TMO from the oxidation of Mn^{2+}(aq) was rarely

78   observed in laboratory conditions and its feasibility and mechanism remain a puzzle.

79   Natural semiconducting minerals (such as metal oxides and sulfides) are widespread in

80   nature and capable of direct redox reactions at conduction or valence band via photo-excitation.[46]

81   Although evidence for the direct heterogeneous photocatalysis of Mn^{2+}(aq) (i.e., oxidation through

82   the electron transfer from Mn^{2+}(aq) to valence band of natural semiconducting mineral) is lacking,

83   it is thermodynamically feasible as the valence band position of many natural minerals is higher

4

84 than the reduction potential of Mn(III/IV)/Mn^{2+}(aq). Thus, a photo-excited hole in a valence band

85 is thermodynamically feasible to oxidize Mn^{2+}(aq). A recent observation on the photon-to-electron

86 conversion by natural semiconducting minerals on rock surfaces supports the potential of mineral

87 photocatalysis and the subsequent direct photocatalytic oxidation of Mn^{2+}(aq) by natural

88 semiconducting minerals.[47] A recent study described the oxidation of Mn^{2+}(aq) on natural

89 semiconducting minerals (Fe and Ti oxides), but the high concentration of Mn^{2+}(aq) (14 mM) used

90 in the study was not representative of natural conditions.[48] Systematic studies are thus desired to

91 further explore the reaction kinetics and mechanisms of mineral catalyzed photocatalytic oxidation

92 of Mn^{2+}(aq) under environmentally relevant conditions, as well as the structure of the formed Mn

93 oxides.

94 In natural systems, one of the most photoreactive semiconducting minerals is TiO_2. Ti is

95 the 9th most abundant element in Earth's crust, and rutile is the most commonly occurring structure

96 of natural TiO_2.[49] Anatase is a polymorph of TiO_2.[50, 51] Due to their strong photoreactivity, both

97 rutile and anatase nanoparticles are used extensively in photocatalytic energy and environmental

98 applications.[46, 51-53] Because of the widespread anthropogenic use of TiO_2 in the last two decades,

99 many studies have reported rapidly increasing concentrations of engineered TiO_2 nanoparticles in

100 surface waters and wastewater treatment systems.[53-57] While extensive studies have been

101 conducted to evaluate the toxicity of TiO_2 nanoparticles in nature, their photocatalytic effects on

102 natural redox cycles remains elusive. Thus, investigating the roles of TiO_2 minerals in the

103 photocatalytic oxidation of Mn^{2+} and formation of Mn oxides have important implications for both

104 natural and engineered systems.

105 In this study, we show rapid photocatalytic oxidation of Mn^{2+}(aq) in the presence of rutile

106 and anatase (representing natural minerals and emerging engineered nanoparticles of TiO_2,

107 respectively). The observed oxidation rates are comparable to or even faster than currently known

108 biotic processes. In addition, we show that the direct formation of TMO with large tunnel size,

109 such as todorokite (3 × 3) and romanechite (2 × 3), occurs via heterogeneous nucleation on the

110 surface of TiO_2. Considering the abundance of natural semiconducting minerals, our findings

111 confirm the importance of direct photocatalytic oxidation for explaining the oxidation of Mn(II)

112 and the formation and diversity of Mn oxides in environmental systems. These results also point

113 to the potential influence of environmental nanoparticles on natural element and electron cycles.

114

115 **2. EXPERIMENTAL SECTION**

116 **Materials and reagents**

117 Rutile and anatase TiO_2 phases were obtained from Alfa Aesar and were confirmed phase

118 pure by X-ray diffraction (XRD). Their specific surface areas were measured by using Brunauer–

119 Emmett–Teller (BET) method with N_2 gas adsorption (Autosorb-1-MP surface pore analyzer,

120 Quantachrome Corp.) and are 5.5 m^2/g for rutile and 51.5 m^2/g for anatase. $MnCl_2$ stock solution

121 was used to achieve 100 μM Mn^{2+}(aq) in artificial sea water (ASW) and deionized water (DI).

122 ASW was prepared with 0.42 M NaCl, 0.025 M $MgSO_4$, 0.0091 M $CaCl_2$, 0.0089 M KCl, and

123 0.0024 M $NaHCO_3$.[58] The pH value of the ASW experiments remained at 7.9 ± 0.1 during the 8 h

124 reaction without any adjustment. The pH value in the DI experiments was initially adjusted to 7.5

125 ± 0.1 and later adjusted every hour using dilute NaOH or HCl. Throughout the reaction, pH stayed

126 within the range of 7.5–7.8. TiO_2 particles (0.1 g/L) were dispersed in 180 mL ASW or DI

127 solutions and sonicated for 10 min before starting the photocatalytic reactions. To understand the

128 effect of cations on the rapid photocatalytic oxidation and formation of tunnel structured Mn

129 oxides, parallel experiments were conducted by reacting anatase particles in DI water containing

6

130   only one cation (0.42 M NaCl, 0.025 M MgSO$_4$, or 0.0091 M CaCl$_2$; consistent with their

131   corresponding concentrations in ASW). The suspension pH was initially adjusted to 7.5 ± 0.1, was

132   adjusted every hour, and stayed within the range of 7.5–7.8 throughout the experiments. These

133   experiments are referred to as single cation experiments.

134

135   **Photocatalytic oxidation of Mn^{2+}(aq)**

136   Photochemical experiments were initiated by illuminating the prepared TiO$_2$ suspension

137   by a 450 W Xe-arc lamp light source (Newport). The light passed through a 10 cm IR water filter

138   to avoid the increase of temperature. We used a borosilicate reactor with a quartz window (1 inch

139   diameter) facing the light. The reaction suspension was magnetically stirred over the entire

140   reaction process. Aliquots (0.3 mL) of the suspension was taken every hour to analyze the

141   concentration of oxidized Mn(III,IV) using the leucoberbelin blue (LBB, Sigma Aldrich)

142   colorimetric method at 625 nm on an UV-vis spectrophotometer (Cary 60, Agilent). Calibration

143   of the LBB method used KMn^{VII}O$_4$.[59] Because 1 mole of Mn(VII) oxidizes 5 moles of LBB, using

144   the obtained calibration with Mn(VII), the amount of oxidized Mn^{2+} can be converted to Mn(III)

145   or Mn(IV) equivalent by considering the oxidation state of Mn oxides. For example, 10 µM

146   Mn(VII) is equivalent to 25 µM Mn(IV) or 50 µM Mn(III). Because it is difficult to accurately

147   determine the oxidation state of the photochemically formed Mn oxides, we used Mn(III)

148   equivalent calculation in order to compare the electron flow under different reaction conditions.

149   All experiments were conducted in replicates.

150   Several control experiments were also conducted by using anatase in ASW, as this system

151   showed the fastest oxidation among all tested conditions. (1) Dark experiments were conducted to

152   differentiate photocatalytic oxidation (i.e., Mn(II) oxidation by photochemically generated holes)

153   from mineral surface catalyzed oxidation (i.e., heterogeneous Mn(II) oxidation by molecular

154   oxygen on mineral surface[60, 61]). (2) To determine the photoactive wavelength region of anatase

155   for Mn^{2+}(aq) oxidation, 400 or 550 nm optical cut-off filters (Newport) was used to cut-off lights

156   lower than 400 or 550 nm wavelength, respectively. The optical filter was placed between the light

157   source and reactor. Because anatase showed much higher oxidation rate as compared to rutile, the

158   control experiment was conducted using anatase to clearly distinguish the effective wavelength

159   region for the photocatalytic oxidation of Mn^{2+}(aq) by TiO_2. (3) Because TiO_2 can generate

160   superoxide upon photoexcitation[51], to confirm the contribution of superoxide for the oxidation of

161   Mn^{2+}(aq), scavenge experiments were conducted by adding 0.1 µM superoxide dismutase (SOD,

162   Sigma Aldirch) in the suspension to scavenge superoxide during the reaction. (4) A control

163   experiment was conducted in the absence of TiO_2, which showed no oxidation of Mn^{2+}(aq) in both

164   ASW and DI water conditions.

165

166   **Calculation of quantum yield**

167   Using the photocatalytic oxidation of Mn^{2+}(aq) by TiO_2 with 450 W Xe-arc lamp, we

168   calculated the quantum yield of rutile and anatase in ASW and DI. Multiplying irradiance of 450

169   W Xe-arc lamp (Figure S1), wavelength, unit conversion factor, absorbance at each wavelength

170   provides photons generated by a certain wavelength of 450 W Xe-arc lamp light. The exposed area

171   and penetration depth were multiplied in the reactor. To obtain total photons generated by anatase

172   or rutile by 450 W Xe-arc lamp, the calculated number of photons per wavelength using Equation

173   1 below were integrated from 250 to 800 nm (Table S4).

174

175   $I \left(\frac{photons}{nms} \right) = I(W/cm^2 nm) \times Wavelength(nm) \times 5.035 \times 10^{15}(photons/s \cdot nm) \times$

176     $Abs.(1/cm) \times penetration\ depth\ (cm) \times area\ (cm^2)$ Eq. (1)

177

178   We used the concentration of Mn(III) equivalent, which represents successfully transferred holes

179   from TiO_2. Because the Mn(III) equivalent concentration reached a plateau after 6 h for reaction

180   in rutile suspension, we used the concentration at 6 h for the calculation of quantum yield.

181

182     $QY\ (\%) = \dfrac{total\ oxidized\ Mn^{2+}(aq)\ for\ 6\ hrs}{total\ generated\ photons\ from\ TiO_2\ for\ 6\ hrs} \times 100$ Eq. (2)

183

184   Using the obtained quantum yields of TiO_2 in ASW and DI, we obtained the estimated oxidation

185   rates of Mn^{2+}(aq) by TiO_2 under natural sunlight exposure. The spectrum of natural sunlight

186   (reference E-490-00; Figure S1) is obtained from the National Renewable Energy Laboratory.

187   Using Equation 1 and integration, the total number of photons were obtained under sunlight

188   irradiation. By multiplying the total number of photons and quantum yield, we obtained the

189   estimated concentration of Mn(III) equivalent under sunlight irradiation in 6 h reaction. The

190   oxidation rates under sunlight condition were estimated by linearizing the Mn(III) equivalent

191   concentration between 0 and 6 h.

192

193   **Characterization of heterogeneously nucleated Mn oxides on TiO_2**

194   At each time point, the reacted suspension was syringe filtered (0.2 µm) and analyzed by

195   LBB colorimetric method to quantify the amount of Mn oxides formed on the surface of TiO_2

196   (heterogeneous nucleation) and in the solution (homogeneous nucleation). To identify the phase

197   and oxidation state of Mn oxides, reacted solids were collected at the end of photocatalysis by

198   repeated centrifugation and rinsing by DI water, followed by freeze-drying. The dried samples

199 were analyzed using X-ray photoelectron spectroscopy (XPS), synchrotron XRD (SXRD), and

200 synchrotron X-ray absorption spectroscopy (XAS), as detailed below.

201   Mn 3p XPS spectra, which show better sensitivity of Mn oxidation state than Mn 2p

202 spectra[62, 63], was obtained on a K-alpha XPS system with monochromatic Al Kα radiation (1486.6

203 eV) (ThermoFisher Scientific). Although Mn 3s spectra are also useful for analyzing Mn oxidation

204 state, the use of Mn 3s in this study was inappropriate due to its overlap with Mg 1s spectra for

205 ASW samples. Energy calibration used C 1s spectra (284.6 eV). Fitting of Mn 3p spectra was

206 conducted with allocations of Mn(II), Mn(III), and Mn(IV) at 47.8, 48.6, and 49.8 eV, respectively.

207   SXRD was measured at Beamline 17-BM-B (51.324 keV, $\lambda = 0.24157$ Å) at the Advanced

208 Photon Source (APS, Lemont, IL, US). Mn K-edge X-ray absorption spectroscopy (XAS) analysis

209 was conducted at Beamline 4-1 at the Stanford Synchrotron Radiation Lightsource (SSRL, Menlo

210 Park, CA, US), Beamline 12-BM-B at APS, and Beamline 6-BM at National Synchrotron Light

211 Source-II (NSLS-II, Upton, NY, US). Both XANES (X-ray absorption near edge structure) and

212 EXAFS (extended X-ray absorption fine structure) data were collected. The monochromators were

213 detuned by 40% to avoid higher order harmonics. Energy calibration used Mn foil. Multiple scans

214 (2–6) were collected for each sample, averaged, and normalized for further analysis. Analysis of

215 the Mn XANES spectra for each sample showed no evidence of photo-reduction under the X-ray

216 beam.

217   XAS data analysis was performed using the programs SIXPACK [64] and Ifeffit [65]. Linear

218 combination fitting (LCF) of the Mn XANES region was conducted to determine the relative

219 percentage of Mn(II), Mn(III), and Mn(IV) species and the average oxidation state (AOS)

220 following previous procedures.[66] To obtain statistically meaningful fitting results, all possible

221 combinations were fitted with at most four references among 12 references in Table S1. Among

222 the obtained 781 different fitting results, 30 fitting results with the lowest R factors were selected

223 and averaged to determine AOS and percentages of Mn valence states. Considering the typical 10%

224 error for LCF, values lower than 5% were considered negligible. Details on the reference

225 compounds and results for LCF analysis are in Table S1 and Table S2, respectively.

226

227 **3. RESULTS AND DISCUSSION**

228 **Rapid photocatalytic oxidation of Mn^{2+}(aq)**

229 In the presence of TiO_2 minerals, Mn^{2+}(aq) in both ASW and DI was quickly oxidized

230 (Figure 1). The oxidation rates with different mineral phases and aqueous conditions (1.4 to 8.0

231 μM hr^{-1}) (Figure S2) are all comparable to or faster than those of biotic processes ($\sim 1.2 \pm 0.2$ μM

232 hr^{-1}) [37, 67-69]. This finding suggests that photocatalytic oxidation of Mn^{2+}(aq) by TiO_2 is a feasible

233 scenario in nature due to the abundance of natural semiconducting TiO_2 minerals[49] and increasing

234 concentrations of anthropogenic nanoparticles in environmental systems.[53-57, 70] Indiscernible

235 oxidation under dark condition indicates that both surface catalyzed oxidation of Mn^{2+}(aq) by TiO_2

236 (i.e., heterogeneous oxidation) and homogeneous oxidation of Mn^{2+}(aq) by dissolved oxygen in

237 solutions are negligible compared to photocatalytic oxidation (Figure S3). Anatase shows about

238 two times faster oxidation rates than rutile in both ASW and DI (Figure 1 and Figure S2). This

239 difference might be from the higher specific surface area of anatase (51.5 m^2 g^{-1}) than rutile (5.5

240 m^2 g^{-1}). However, surface area normalized concentrations of Mn(III) equivalent showed that the

241 oxidized Mn^{2+}(aq) is about an order of magnitude higher on the surface of rutile than that of anatase

242 (Figure S4), indicating that the difference of surface area might not be the dominant controlling

243 factor for the higher oxidation rates in anatase suspensions. This suggests that the higher oxidation

244 rates in anatase suspensions is likely due to the higher photo-reactivity of anatase for redox

245   reaction.[51]

246   Except for the photocatalytic oxidation of Mn^{2+}(aq) in ASW-anatase suspension, all other

247   conditions showed slowed oxidation after 6 h (Figure 1). This is possibly due to the aggregation

248   of TiO_2 particles over time, attachment of TiO_2 particles to the photochemical reactor over time,

249   or the blockage of surface active sites by the nucleated Mn oxide.

250   Interestingly, both anatase and rutile show faster oxidation in ASW than that in DI. The

251   pH difference in ASW (7.9 ± 0.1) vs DI (7.5−7.8) might partially contribute to the difference in

252   oxidation rate. Our thermodynamic calculations using Visual MINTEQ showed no significant

253   changes in Mn(II) aqueous speciation in ASW and DI conditions (data not shown). Thus we

254   hypothesize that the difference in oxidation rate is likely due to the presence of large amount of

255   cations (e.g., Na^+, K^+, Ca^{2+}, and Mg^{2+}) in ASW that can facilitate the oxidation of Mn^{2+}(aq) and

256   formation of Mn oxides.[44, 71, 72] This is confirmed by the single cation experiments using solutions

257   containing only one cation at the corresponding ASW concentration (i.e. 0.091 M Ca^{2+}, 0.025 M

258   Mg^{2+}, or 0.420 M Na^+). The photocatalytic oxidation of Mn^{2+}(aq) by anatase in single cation

259   experiments with Mg^{2+} (~8.2 $\mu M\ hr^{-1}$) or Ca^{2+} (~6.6 $\mu M\ hr^{-1}$) (Figure S5A) shows oxidation rates

260   similar to ASW systems (8.0 ± 0.6 $\mu M\ hr^{-1}$). Interestingly, in single cation experiment with Na^+,

261   we observed the fastest oxidation rate (~11.3 $\mu M\ hr^{-1}$) among all the tested experimental conditions.

262   This indicates the profound role of cations in the photocatalytic oxidation and formation of Mn

263   oxides on TiO_2 particles. The different phase of Mn oxides formed in the single cation experiments

264   (Figure 2) also supports the influence of cations on the Mn oxide structure, as discussed below.

265   Since this study focuses on the photocatalytic oxidation of Mn^{2+}(aq) by TiO_2 nanoparticles and

266   consequent formation of TMO, detailed mechanistic understanding of the roles of cations and

267   anions in the oxidation rate is beyond the scope of this work. Further studies are warranted to

268   explain the photocatalytic reactions of TiO_2 under varied aqueous conditions.

269

Formation of large tunnel structured Mn oxides

271   The rapid photocatalytic oxidation of Mn^{2+}(aq) led to the formation of Mn oxides on the

272   surface of TiO_2. Mn(III,IV) species were not detected by the LBB method in the filtrate of the

273   reaction suspension at all times (Figure S3). Considering that homogeneously nucleated Mn oxides

274   are 6–30 nm in diameter,[73] which can readily pass through 0.22 µm filters, the absence of Mn

275   oxides at all times in the filtrate likely indicates the heterogeneous nucleation of Mn oxides on the

276   surface of TiO_2 instead of homogeneous nucleation of Mn oxide nanoparticles in solution.

277   Interestingly, we also observed the formation of TMO with large tunnels under all reaction

278   conditions (Figure 2A and 2B). Considering that LMO (such as δ-MnO_2 and birnessite) are the

279   typical phase of homogeneously nucleated Mn oxides through biotic/abiotic processes,[36, 37, 74] the

280   formation of TMO in our system also strongly suggest the heterogeneous nucleation of Mn oxides

281   on TiO_2 through photocatalytic oxidation of Mn^{2+}(aq). SXRD analyses of the 8-h samples in

282   anatase-ASW and rutile-ASW suspensions (Figure 2A and 2B) indicate the formation of

283   todorokite (3×3 tunnel size) with diffraction peaks at 9.6 and 4.8 Å d-spacing. Although the large

284   d-spacing can also occur from buserite, which has similar structure to birnessite but with a 10 Å

285   interlayer spacing, the interlayer of buserite (10 Å interlayer spacing) collapses to birnessite (~7 Å

286   interlayer spacing) upon dehydration due to weakly bound interlayer H_2O in the interlayer

287   positions [40, 75, 76]. Thus, the large d-spacing of our fully dehydrated samples (obtained under

288   vacuum freeze-drying for 1 day) indicates that the nucleated Mn oxide on TiO_2 in ASW is

289   todorokite. In anatase-DI and rutile-DI suspensions, SXRD showed only weak diffraction at ~4.9

290   Å, which occurs from all large tunnel structured Mn oxides (3×3, 3×2, and 2×2 tunnel size)

291 (Figure 2A and 2B). To further identify the structure of the Mn oxides formed in DI experiments,

292 we conducted Mn K-edge EXAFS analysis and identified the formation of romanechite-like

293 structure (2×3 tunnel size) (Figure 2C). Specifically, the region between 7 and 10 Å^{-1} in k space

294 is a well-known "indicator region" for Mn oxide structure.[77, 78] In this region, Mn oxides formed

295 in DI experiments have two peaks at ~8.7 and 9.2 Å^{-1}, consistent with the spectra of romanechite

296 and is distinctively different from the spectra of todorokite formed in ASW (Figure 2C) and

297 hollandite (2×2 tunnel size, Figure S6). These results indicate an important observation that

298 heterogeneous nucleation on natural mineral surfaces can facilitate the direct formation of TMO

299 with large tunnels. Specifically, todorokite is one of the most ubiquitous natural Mn oxides, yet its

300 formation in low temperature environments is poorly constrained due to the difficulties in

301 synthesizing this phase in laboratory settings through the transformation of LMO to TMO. Most

302 previous studies employed reaction conditions that do not represent circumneutral low temperature

303 environments, such as the transformation of Mg^{2+}-intercalated LMO using reflux or hydrothermal

304 reactions at temperatures above 100 °C [41, 42, 44]. Our findings suggest that photocatalytically

305 promoted direct heterogeneous nucleation of Mn oxides on natural minerals might be an alternative

306 pathway for the formation of todorokite. In our system, the underlying TiO_2 minerals serve as

307 templates to facilitate the heterogeneous nucleation of Mn oxides, which might have lowered the

308 structural strain and formation energy for TMO. In addition, this observation also suggest a new

309 phase selection pathway (i.e., formation of TMO via heterogeneous nucleation of Mn oxides) as

310 compared to previously observed common formation of LMO induced by homogeneous nucleation

311 of Mn oxides upon Mn(II) oxidation [36, 37, 74]. Future microscopic studies are warranted to further

312 investigate the mechanism, structure, and morphology of the heterogeneously nucleated TMO,

313 such as the use of high resolution transmission electron microscopy (HRTEM) to analyze the

314   micromorphology, potential presence of poorly crystalline LMO, and relationships with the

315   mineral substrate.

316   Prior studies showed the importance of Mn(III) and large cations (e.g., Mg^{2+}, Ca^{2+}) on the

317   transformation of LMO to TMO with large tunnels.[41, 42, 44, 71, 79-81] In our system, Mn oxides

318   produced from all tested conditions contain considerable amount of structural Mn(III) as probed

319   by XPS and XANES (Figures 3 and S7 and Table S2), which is necessary to form TMO. The

320   results show that Mn oxides formed in the presence of anatase have more Mn(III) in the structure

321   than those formed in the rutile system. Specifically, Mn oxides formed in the anatase-ASW

322   suspension show a higher content of Mn(III) than those formed in rutile-ASW suspension based

323   on the fitting of Mn 3p XPS spectra. This feature can be readily observed from the lower peak

324   position of Mn 3p spectra of anatase-ASW sample than that of rutile-ASW (Figure 3). It is worth

325   noting that obtaining accurate ratios of Mn(III/IV) using XPS and XANES is challenging, due to

326   errors resulting from data fitting and the intrinsic differences in these techniques (i.e., XANES

327   obtains bulk information whereas XPS detects near-surface structure).[82] Nonetheless, linear

328   combination fitting (LCF) of Mn XANES spectra also shows that the nucleated Mn oxides in

329   anatase-ASW suspension have higher content of Mn(III) than those formed in rutile-ASW

330   suspension (Figure S7 and Table S2). Despite the difference in Mn(III) content, the Mn oxides

331   formed in both anatase and rutile suspensions have the same structure (i.e., todorokite in ASW and

332   romanechite in DI).

333   Interestingly, although the Mn oxides formed in rutile-DI and rutile-ASW suspensions

334   show similar Mn(III) contents, they have different structures. This suggests that the observed

335   different tunnel sizes between ASW (todorokite, 3×3) and DI (romanechite, 2×3) systems mainly

336   resulted from the presence of cations in ASW, not from the difference in Mn(III) content. Indeed,

337   results from the single cation experiments (DI water containing only Mg^{2+}, Ca^{2+}, or Na^+ at their

338   corresponding ASW concentrations) support the relative importance of different cations in ASW

339   in mediating the TMO formation. Among all anatase-single cation experiments (Mg^{2+}, Ca^{2+}, or

340   Na^+), the Mn oxides produced in Mg^{2+} experiment shows the most relevant structure to Mn oxide

341   formed in anatase-ASW suspension, as revealed by linear combination fitting of Mn K-edge

342   EXAFS spectra (Figure S5B and Table S3). This observation is consistent with prior studies

343   showing the necessity of Mg^{2+} intercalation into LMO to enable the hydrothermal transformation

344   of LMO to todorokite.[41, 42, 44, 71, 79-81] Ca^{2+} also likely contributes to the formation of todorokite,

345   based on the similarity in EXAFS indicator region for Mn oxides produced in the Ca^{2+} single cation

346   experiment as compared to todorokite spectra. We can rule out the contribution of Na^+ to the

347   formation of todorokite in ASW based on the formation of romanechite-like structure (Figure S5B

348   and Table S3). Overall, results from the single cation experiments indicate that, regardless of the

349   mineral catalyst, large cations (e.g., Mg^{2+} and Ca^{2+}) in ASW are main factors responsible for the

350   structural difference during heterogeneous nucleation of Mn oxide on TiO_2 in ASW vs DI water.

351   Detailed mechanistic investigation on the effects of cations on the oxidation of Mn^{2+}(aq) and the

352   structure of nucleated Mn oxides is beyond the scope of this study and warrants further work.

353

354   **Reaction mechanisms**

355   Our mechanistic study further reveals that photo-excitation of TiO_2 enables the rapid

356   oxidation of Mn^{2+}(aq) by the generation of (1) holes at valence band (direct oxidation) as well as

357   (2) superoxide (indirect oxidation), as explained below.

358   For Mn^{2+} oxidation by the generated holes at valence band (direct oxidation): we conducted

359   parallel experiments using different optical cut-off filters in the anatase-ASW suspension (which

16

360   shows the fastest oxidation) to elucidate the mechanisms of photocatalytic oxidation of Mn^{2+}(aq).

361   We found that the rapid oxidation occurs via the photo-excitation of electrons and holes from

362   anatase (Figure 4A). Specifically, in the presence of 400 nm cutoff optical filter (which cuts off

363   wavelengths at < 400 nm), the oxidation of Mn^{2+}(aq) is significantly suppressed. This indicates

364   that the rapid oxidation of Mn^{2+}(aq) occurs mainly from the photo-excitation in UVA region (320–

365   400 nm), which matches the band-gap of anatase (3.2 eV). With 550 nm cutoff optical filter (cutoff

366   < 550 nm), little oxidation of Mn^{2+}(aq) occurred (Figure 4A) due to completely suppressed photo-

367   excitation.

368   For Mn^{2+} oxidation by superoxide (indirect oxidation): TiO_2 is capable of generating

369   superoxide because its conduction band located at lower reduction potential than that of oxygen

370   (O_2) / superoxide (O_2^-) (Figure 4C). Prior studies show that superoxide can readily oxidize Mn^{2+}(aq)

371   while hydroxyl radical and hydrogen peroxide cannot.[36, 68] In our control experiment with

372   superoxide scavenger SOD, both the extent and rate of Mn^{2+} oxidation decreased slightly,

373   indicating the contribution of superoxide (produced from photocatalysis) in the indirect oxidation

374   of Mn^{2+} (Figure 4D). However, considering the small decrease in Mn^{2+} oxidation caused by SOD

375   as compared to those caused by the cut-off filters (Figure 4D), direct electron transfer from

376   Mn^{2+}(aq) to photo-generated holes is still considered as the dominant oxidation mechanism. In

377   addition, the occurrence of superoxide and the observed direct electron transfer from Mn^{2+}(aq) to

378   a hole in the valence band of TiO_2 indicate that oxygen is the electron acceptor which suppresses

379   the recombination between the photo-generated electrons and holes.

380

381   **4. ENVIRONMENTAL IMPLICATIONS**

382   To assess the relative importance of this photocatalytic oxidation process in nature, we

383 compare the oxidation rates obtained from this study to previously observed representative

384 oxidation rates. Using the experimentally obtained photocatalytic oxidation rate, spectra of 450 W

385 Xe-arc lamp and natural sunlight, and by calculating the quantum yields (Table S4 and Figure S1),

386 we extrapolated the laboratory oxidation rates (450 W Xe lamp) to natural sunlight condition. We

387 note that oxidation processes are controlled by many factors (e.g., pH, initial Mn^{2+} concentration,

388 dissolved oxygen concentration, temperature, solution chemistry, etc.). Nevertheless, the

389 comparison of oxidation rates in Figure 5 provides an initial visual comparison of the relative

390 importance of different oxidation pathways. As shown in the experimental and calculated results

391 with TiO_2 (Figure 5), the calculated oxidation rates under natural sunlight condition are

392 comparable to or faster than that of microbial oxidation processes. Natural semiconducting

393 minerals occur in a wide variety of natural systems. Besides TiO_2 and Fe oxides, other natural

394 semiconducting minerals such as ZnS, FeS, etc. may also serve to photocatalytically oxidize

395 Mn^{2+}(aq) (or other species). However, different mineral catalysts might insert different

396 photocatalytic oxidation mechanisms.

397   Our findings highlight the importance of a previously overlooked pathway: the

398 photocatalytic oxidation of Mn^{2+}(aq), which might significantly contribute to Mn redox balance in

399 nature. Meanwhile, the observed fast photocatalytic oxidation of Mn^{2+}(aq) raises the potential

400 concern of semiconducting nanoparticles in influencing environmental redox systems. Through

401 anthropogenic activities, TiO_2 and other semiconducting nanoparticles are released to a wide

402 variety of environmental systems. Based on the observed rapid photocatalytic oxidation by TiO_2

403 in this study, accumulation of the photo-active nanoparticles in nature might influence the balance

404 of Mn redox. As an example of such anthropogenic impact, a recent study reported the occurrence

405 of elevated concentration of dissolved Mn from the reduction of natural Mn oxides by emerging

406 contaminants and fertilizers in US groundwater, impacting more than 2.6 million people

407 consuming the Mn contaminated groundwater.[83] In contrary, the increase of semiconducting

408 nanoparticles in environmental systems might promote the oxidation of Mn^{2+}(aq) and formation

409 of Mn oxides, thus affecting the fate and transport of many other elements and contaminants. For

410 example, Mn oxides are known to oxidize the more mobile As(III) into the less mobile As(V)

411 species, whereas they can oxidize the less mobile Cr(III) species into more mobile and toxic Cr(VI)

412 species [3, 84-87].

413   This study also demonstrates the direct formation of todorokite through heterogeneous

414 nucleation on the surface of natural minerals under circumneutral conditions in the presence of

415 large cations. To our knowledge, this is the first observation of direct formation of todorokite in

416 laboratory settings under environmentally relevant conditions (Table S5). The results suggest that

417 environmental conditions, such as solution chemistry, mineral surface, etc., may govern the

418 polymorphism of natural Mn oxides, and the latter in turn might potentially serve as a fingerprint

419 to trace environmental conditions at the time of Mn oxide formation.

ASSOCIATED CONTENT

Supporting Information.

Reference compounds used for XANES LCF (Table S1), results of XANES LCF (Table S2), results of EXAFS LCF (Table S3), results on the calculation of quantum yields (Table S4), experimental conditions of the representative biotic/abiotic oxidation of Mn^{2+}(aq) to Mn(IV) (Table S5), irradiance spectra of Xe-arc lamp and sunlight (Figure S1), linear initial oxidation rates (Figure S2), results of dark and filtrate control test (Figure S3), surface area normalized concentration of Mn(III) equivalent (Figure S4), effect of cations on the photocatalytic oxidation rates (Figure S5), EXAFS spectra of the nucleated Mn oxides and references (Figure S6), and XANES data (Figure S7).

References

1.   Sunda, W. G.; Kieber, D. J., Oxidation of humic substances by manganese oxides yields low-molecular-weight organic substrates. *Nature* **1994,** *367*, (6458), 62-64.

2.   Stone, A. T.; Morgan, J. J., Reduction and dissolution of manganese (III) and manganese (IV) oxides by organics: 2. Survey of the reactivity of organics. *Environ. Sci. Technol.* **1984,** *18*, (8), 617-624.

3.   Fendorf, S. E.; Zasoski, R. J., Chromium(III) oxidation by d-manganese oxide (MnO_2). 1. Characterization. *Environ. Sci. Technol.* **1992,** *26*, (1), 79-85.

4.   Murray, K. J.; Webb, S. M.; Bargar, J. R.; Tebo, B. M., Indirect oxidation of Co (II) in the presence of the marine Mn (II)-oxidizing bacterium Bacillus sp. strain SG-1. *Appl. Environ. Microbiol.* **2007,** *73*, (21), 6905-6909.

5.   Nealson, K. H.; Saffarini, D., Iron and manganese in anaerobic respiration: environmental significance, physiology, and regulation. *Annu. Rev. Microbiol.* **1994,** *48*, (1), 311-343.

6.   Lefkowitz, J. P.; Rouff, A. A.; Elzinga, E. J., Influence of pH on the Reductive Transformation of Birnessite by Aqueous Mn(II). *Environ. Sci. Technol.* **2013,** *47*, (18), 10364-10371.

7.   Wang, Z.; Xiong, W.; Tebo, B. M.; Giammar, D. E., Oxidative UO_2 Dissolution Induced by Soluble Mn (III). *Environ. Sci. Technol.* **2013,** *48*, (1), 289-298.

8.   Wang, Z.; Tebo, B. M.; Giammar, D. E., Effects of Mn (II) on UO_2 Dissolution under Anoxic and Oxic Conditions. *Environ. Sci. Technol.* **2014,** *48*, (10), 5546–5554.

9.   Elzinga, E. J., 54Mn Radiotracers Demonstrate Continuous Dissolution and Reprecipitation of Vernadite (δ-MnO_2) during Interaction with Aqueous Mn(II). *Environ. Sci. Technol.* **2016,** *50*, (16), 8670-8677.

10.   Borch, T.; Kretzschmar, R.; Kappler, A.; Cappellen, P. V.; Ginder-Vogel, M.; Voegelin, A.; Campbell, K., Biogeochemical redox processes and their impact on contaminant dynamics. *Environ. Sci. Technol.* **2009,** *44*, (1), 15-23.

11.   Villalobos, M.; Toner, B.; Bargar, J.; Sposito, G., Characterization of the manganese oxide produced by Pseudomonas putida strain MnB1. *Geochim. Cosmochim. Acta* **2003,** *67*, (14), 2649-2662.

12.   Zhao, S.; Wang, Q.; Sun, J.; Borkiewicz, O. J.; Huang, R.; Saad, E. M.; Fields, B.; Chen, S.; Zhu, M.; Tang, Y., Effect of Zn coprecipitation on the structure of layered Mn oxides. *Chem. Geol.* **2018,** *493*, (20), 234-245.

13.   Planavsky, N. J.; Asael, D.; Hofmann, A.; Reinhard, C. T.; Lalonde, S. V.; Knudsen, A.; Wang, X.; Ossa Ossa, F.; Pecoits, E.; Smith, A. J. B.; Beukes, N. J.; Bekker, A.; Johnson, T. M.; Konhauser, K. O.; Lyons, T. W.; Rouxel, O. J., Evidence for oxygenic photosynthesis half a billion years before the Great Oxidation Event. *Nat. Geosci.* **2014,** *7*, (4), 283-286.

14.   Daye, M.; Klepac-Ceraj, V.; Pajusalu, M.; Rowland, S.; Farrell-Sherman, A.; Beukes, N.; Tamura, N.; Fournier, G.; Bosak, T., Light-driven anaerobic microbial oxidation of manganese. *Nature* **2019,** *576*, (7786), 311-314.

15.   Lingappa, U. F.; Monteverde, D. R.; Magyar, J. S.; Valentine, J. S.; Fischer, W. W., How manganese empowered life with dioxygen (and vice versa). *Free Radical. Biol. Med.* **2019,** *140*, 113-125.

16.   Lanza, N. L.; Wiens, R. C.; Arvidson, R. E.; Clark, B. C.; Fischer, W. W.; Gellert, R.; Grotzinger, J. P.; Hurowitz, J. A.; McLennan, S. M.; Morris, R. V.; Rice, M. S.; Bell III, J. F.; Berger, J. A.; Blaney, D. L.; Bridges, N. T.; Calef III, F.; Campbell, J. L.; Clegg, S. M.; Cousin,

A.; Edgett, K. S.; Fabre, C.; Fisk, M. R.; Forni, O.; Frydenvang, J.; Hardy, K. R.; Hardgrove, C.; Johnson, J. R.; Lasue, J.; Le Mouélic, S.; Malin, M. C.; Mangold, N.; Martìn-Torres, J.; Maurice, S.; McBride, M. J.; Ming, D. W.; Newsom, H. E.; Ollila, A. M.; Sautter, V.; Schröder, S.; Thompson, L. M.; Treiman, A. H.; VanBommel, S.; Vaniman, D. T.; Zorzano, M.-P., Oxidation of manganese in an ancient aquifer, Kimberley formation, Gale crater, Mars. *Geophys. Res. Lett.* **2016,** *43*, (14), 7398-7407.

17.   Wang, Y.; Benkaddour, S.; Marafatto, F. F.; Peña, J., Diffusion- and pH-Dependent Reactivity of Layer-Type MnO2: Reactions at Particle Edges versus Vacancy Sites. *Environ. Sci. Technol.* **2018,** *52*, (6), 3476-3485.

18.   Droz, B.; Dumas, N.; Duckworth, O. W.; Peña, J., A Comparison of the Sorption Reactivity of Bacteriogenic and Mycogenic Mn Oxide Nanoparticles. *Environ. Sci. Technol.* **2015,** *49*, (7), 4200-4208.

19.   Remucal, C. K.; Ginder-Vogel, M., A critical review of the reactivity of manganese oxides with organic contaminants. *Environ. Sci.: Process. Impacts* **2014,** *16*, (6), 1247-1266.

20.   Balgooyen, S.; Alaimo, P. J.; Remucal, C. K.; Ginder-Vogel, M., Structural transformation of MnO_2 during the oxidation of bisphenol A. *Environ. Sci. Technol.* **2017,** *51*, (11), 6053-6062.

21.   Balgooyen, S.; Campagnola, G.; Remucal, C. K.; Ginder-Vogel, M., Impact of bisphenol A influent concentration and reaction time on MnO2 transformation in a stirred flow reactor. *Environ. Sci.: Process. Impacts* **2019,** *21*, (1), 19-27.

22.   Kim, T.; Logan, B. E.; Gorski, C. A., A pH-Gradient Flow Cell for Converting Waste CO2 into Electricity. *Environ. Sci. Technol. Lett.* **2017,** *4*, (2), 49-53.

23.   Fortunato, J.; Peña, J.; Benkaddour, S.; Zhang, H.; Huang, J.; Zhu, M.; Logan, B. E.; Gorski, C. A., Surveying Manganese Oxides as Electrode Materials for Harnessing Salinity Gradient Energy. *Environ. Sci. Technol.* **2020**.

24.   Charbonnet, J. A.; Duan, Y.; van Genuchten, C. M.; Sedlak, D. L., Chemical Regeneration of Manganese Oxide-Coated Sand for Oxidation of Organic Stormwater Contaminants. *Environ. Sci. Technol.* **2018**.

25.   Grebel, J. E.; Charbonnet, J. A.; Sedlak, D. L., Oxidation of organic contaminants by manganese oxide geomedia for passive urban stormwater treatment systems. *Water Res.* **2016,** *88*, 481-491.

26.   Huang, J.; Zhong, S.; Dai, Y.; Liu, C.-C.; Zhang, H. J., Effect of MnO_2 phase structure on the oxidative reactivity toward contaminant degradation. *Environ. Sci. Technol.* **2018,** *52*, 11309-11318.

27.   Zhao, S.; Li, C.; Liu, P.; Huang, R.; Saad, E.; Tang, Y., Zinc Presence during Mineral Formation Affects the Sorptive Reactivity of Manganese Oxide. *Soil Syst.* **2018,** *2*, (2), 19.

28.   van Genuchten, C. M.; Pena, J., Sorption selectivity of birnessite particle edges: a d-PDF analysis of Cd(ii) and Pb(ii) sorption by [small delta]-MnO2 and ferrihydrite. *Environ. Sci.: Process. Impacts* **2016,** *18*, (8), 1030-1041.

29.   Diem, D.; Stumm, W., Is dissolved Mn^{2+} being oxidized by O_2 in absence of Mn-bacteria or surface catalysts? *Geochim. Cosmochim. Acta* **1984,** *48*, (7), 1571-1573.

30.   Morgan, J. J., Kinetics of reaction between O_2 and Mn (II) species in aqueous solutions. *Geochim. Cosmochim. Acta* **2005,** *69*, (1), 35-48.

31.   Wehrli, B.; Friedl, G.; Manceau, A., Reaction rates and products of manganese oxidation at the sediment-water interface. In *Aquatic Chemistry: Interfacial and Interspecies Processes*, Huang, C. P.; Omelia, C. R.; Morgan, J. J., Eds. American Chemical Society: 1995; Vol. 244, pp 111-134.

531 32.   Johnson, C.; Ulrich, M.; Sigg, L.; Imboden, D., A mathematical model of the manganese
532 cycle in a seasonally anoxic lake. *Limnol. Oceanogr.* **1991**, *36*, (7), 1415-1426.
533 33.   Tebo, B. M.; Emerson, S., Effect of oxygen tension, Mn (II) concentration, and temperature
534 on the microbially catalyzed Mn (II) oxidation rate in a marine fjord. *Appl. Environ. Microbiol.*
535 **1985,** *50*, (5), 1268-1273.
536 34.   Vojak, P. W.; Edwards, C.; Jones, M. V., Evidence for microbiological manganese
537 oxidation in the River Tamar estuary, South West England. *Estuar. Coast. Shelf Sci.* **1985,** *20*, (6),
538 661-671.
539 35.   Nico, P. S.; Anastasio, C.; Zasoski, R. J., Rapid photo-oxidation of Mn (II) mediated by
540 humic substances. *Geochim. Cosmochim. Acta* **2002,** *66*, (23), 4047-4056.
541 36.   Jung, H.; Chadha, T.; Kim, D.; Biswas, P.; Jun, Y.-S., Photochemically-assisted Fast
542 Abiotic Oxidation of Manganese and Formation of δ–MnO_2 Nanosheets in Nitrate Solution. *Chem.*
543 *Commun.* **2017,** *53*, 4445-4448.
544 37.   Learman, D.; Wankel, S.; Webb, S.; Martinez, N.; Madden, A.; Hansel, C., Coupled biotic–
545 abiotic Mn (II) oxidation pathway mediates the formation and structural evolution of biogenic Mn
546 oxides. *Geochim. Cosmochim. Acta* **2011,** *75*, (20), 6048-6063.
547 38.   Jung, H.; Chadha, T. S.; Min, Y.; Biswas, P.; Jun, Y.-S., Photochemically-assisted
548 Synthesis of Birnessite Nanosheets and Their Structural Alteration in the Presence of
549 Pyrophosphate. *ACS Sustain. Chem. Eng.* **2017,** *5*, (11), 10624-10632.
550 39.   Zhang, T.; Liu, L.; Tan, W.; Suib, S. L.; Qiu, G.; Liu, F., Photochemical Formation and
551 Transformation of Birnessite: Effects of Cations on Micromorphology and Crystal Structure.
552 *Environ. Sci. Technol.* **2018,** *52*, (12), 6864-6871.
553 40.   Post, J. E., Manganese oxide minerals: Crystal structures and economic and environmental
554 significance. *Proc. Natl. Acad. Sci.* **1999,** *96*, (7), 3447-3454.
555 41.   Feng, X. H.; Zhu, M.; Ginder-Vogel, M.; Ni, C.; Parikh, S. J.; Sparks, D. L., Formation of
556 nano-crystalline todorokite from biogenic Mn oxides. *Geochim. Cosmochim. Acta* **2010,** *74*, (11),
557 3232-3245.
558 42.   Atkins, A. L.; Shaw, S.; Peacock, C. L., Release of Ni from birnessite during
559 transformation of birnessite to todorokite: Implications for Ni cycling in marine sediments.
560 *Geochim. Cosmochim. Acta* **2016,** *189*, 158-183.
561 43.   Yang, P.; Lee, S.; Post, J. E.; Xu, H.; Wang, Q.; Xu, W.; Zhu, M., Trivalent manganese on
562 vacancies triggers rapid transformation of layered to tunneled manganese oxides (TMOs):
563 Implications for occurrence of TMOs in low-temperature environment. *Geochim. Cosmochim.*
564 *Acta* **2018,** *240*, 173-190.
565 44.   Feng, X.; Zhao, H.; Liu, F.; Cui, H.; Tan, W.; Li, W., Transformation from
566 Phyllomanganates to Todorokite under Various Conditions: A Review of Implication for
567 Formation Pathway of Natural Todorokite. In *Advances in the Environmental Biogeochemistry of*
568 *Manganese Oxides*, American Chemical Society: 2015; Vol. 1197, pp 107-134.
569 45.   Jung, H.; Taillefert, M.; Sun, J.; Wang, Q.; Borkiewicz, O. J.; Liu, P.; Yang, L.; Chen, S.;
570 Chen, H.; Tang, Y., Redox Cycling Driven Transformation of Layered Manganese Oxides to
571 Tunnel Structures. *J. Am. Chem. Soc.* **2020,** *142*, (5), 2506-2513.
572 46.   Li, Y.; Ding, C.; Liu, Y.; Li, Y.; Lu, A.; Wang, C.; Ding, H., Visible Light Photocatalysis
573 of Natural Semiconducting Minerals. In *Advances in Photocatalytic Disinfection*, An, T.; Zhao,
574 H.; Wong, P. K., Eds. Springer Berlin Heidelberg: Berlin, Heidelberg, 2017; pp 17-39.
575 47.   Lu, A.; Li, Y.; Ding, H.; Xu, X.; Li, Y.; Ren, G.; Liang, J.; Liu, Y.; Hong, H.; Chen, N.;
576 Chu, S.; Liu, F.; Li, Y.; Wang, H.; Ding, C.; Wang, C.; Lai, Y.; Liu, J.; Dick, J.; Liu, K.; Hochella,

M. F., Photoelectric conversion on Earth's surface via widespread Fe- and Mn-mineral coatings. *Proc. Natl. Acad. Sci.* **2019,** *116*, (20), 9741-9746.

48. Xu, X.; Li, Y.; Li, Y.; Lu, A.; Qiao, R.; Liu, K.; Ding, H.; Wang, C., Characteristics of desert varnish from nanometer to micrometer scale: A photo-oxidation model on its formation. *Chem. Geol.* **2019,** *522*, 55-70.

49. Meinhold, G., Rutile and its applications in earth sciences. *Earth-Sci. Rev.* **2010,** *102*, (1-2), 1-28.

50. Ranade, M. R.; Navrotsky, A.; Zhang, H. Z.; Banfield, J. F.; Elder, S. H.; Zaban, A.; Borse, P. H.; Kulkarni, S. K.; Doran, G. S.; Whitfield, H. J., Energetics of nanocrystalline TiO2. *Proc. Natl. Acad. Sci.* **2002,** *99*, (suppl 2), 6476-6481.

51. Hoffmann, M. R.; Martin, S. T.; Choi, W.; Bahnemann, D. W., Environmental Applications of Semiconductor Photocatalysis. *Chem. Rev.* **1995,** *95*, (1), 69-96.

52. Loeb, S. K.; Alvarez, P. J. J.; Brame, J. A.; Cates, E. L.; Choi, W.; Crittenden, J.; Dionysiou, D. D.; Li, Q.; Li-Puma, G.; Quan, X.; Sedlak, D. L.; David Waite, T.; Westerhoff, P.; Kim, J.-H., The Technology Horizon for Photocatalytic Water Treatment: Sunrise or Sunset? *Environ. Sci. Technol.* **2018**.

53. He, X.; Hwang, H.-M., Engineered TiO2 Nanoparticles: Their Fate and Effects in Natural Aquatic Environments. In 2014; pp 1-20.

54. Rodríguez-Romero, A.; Ruiz-Gutiérrez, G.; Viguri, J. R.; Tovar-Sánchez, A., Sunscreens as a New Source of Metals and Nutrients to Coastal Waters. *Environ. Sci. Technol.* **2019,** *53*, (17), 10177-10187.

55. Weir, A.; Westerhoff, P.; Fabricius, L.; Hristovski, K.; von Goetz, N., Titanium Dioxide Nanoparticles in Food and Personal Care Products. *Environ. Sci. Technol.* **2012,** *46*, (4), 2242-2250.

56. Westerhoff, P.; Song, G.; Hristovski, K.; Kiser, M. A., Occurrence and removal of titanium at full scale wastewater treatment plants: implications for TiO2 nanomaterials. *J. Environ. Monitor.* **2011,** *13*, (5), 1195-1203.

57. Neal, C.; Jarvie, H.; Rowland, P.; Lawler, A.; Sleep, D.; Scholefield, P., Titanium in UK rural, agricultural and urban/industrial rivers: Geogenic and anthropogenic colloidal/sub-colloidal sources and the significance of within-river retention. *Sci. Total Environ.* **2011,** *409*, (10), 1843-1853.

58. Montserrat, F.; Renforth, P.; Hartmann, J.; Leermakers, M.; Knops, P.; Meysman, F. J. R., Olivine Dissolution in Seawater: Implications for CO2 Sequestration through Enhanced Weathering in Coastal Environments. *Environ. Sci. Technol.* **2017,** *51*, (7), 3960-3972.

59. Tebo, B. M.; Clement, B. G.; Dick, G. J., Biotransformations of manganese. *Manual of Environmental Microbiology* **2007,** *3*, 1223-1238.

60. Davies, S. H.; Morgan, J. J., Manganese (II) oxidation kinetics on metal oxide surfaces. *J. Colloid Interface Sci.* **1989,** *129*, (1), 63-77.

61. Junta, J. L.; Hochella Jr, M. F., Manganese (II) oxidation at mineral surfaces: A microscopic and spectroscopic study. *Geochim. Cosmochim. Acta* **1994,** *58*, (22), 4985-4999.

62. Cerrato, J. M.; Hochella Jr, M. F.; Knocke, W. R.; Dietrich, A. M.; Cromer, T. F., Use of XPS to identify the oxidation state of Mn in solid surfaces of filtration media oxide samples from drinking water treatment plants. *Environ. Sci. Technol.* **2010,** *44*, (15), 5881-5886.

63. Cerrato, J. M.; Knocke, W. R.; Hochella, M. F.; Dietrich, A. M.; Jones, A.; Cromer, T. F., Application of XPS and Solution Chemistry Analyses to Investigate Soluble Manganese Removal by MnOx(s)-Coated Media. *Environ. Sci. Technol.* **2011,** *45*, (23), 10068-10074.

64. Webb, S. M., SIXPack a Graphical User Interface for XAS Analysis Using IFEFFIT. *Phys. Scr.* **2005,** *T115*, 1011-1014.

65. Ravel, B.; Newville, M., ATHENA, ARTEMIS, HEPHAESTUS: data analysis for X-ray absorption spectroscopy using IFEFFIT. *J. Synchrotron Radiat.* **2005,** *12*, (4), 537-541.

66. Manceau, A.; Marcus, M. A.; Grangeon, S., Determination of Mn valence states in mixed-valent manganates by XANES spectroscopy. *Am. Mineral.* **2012,** *97*, (5-6), 816-827.

67. Hansel, C. M.; Francis, C. A., Coupled photochemical and enzymatic Mn (II) oxidation pathways of a planktonic Roseobacter-like bacterium. *Appl. Environ. Microbiol.* **2006,** *72*, (5), 3543-3549.

68. Learman, D.; Voelker, B.; Vazquez-Rodriguez, A.; Hansel, C., Formation of manganese oxides by bacterially generated superoxide. *Nat. Geosci.* **2011,** *4*, (2), 95-98.

69. Francis, C. A.; Tebo, B. M., Enzymatic manganese (II) oxidation by a marine α-proteobacterium. *Appl. Environ. Microbiol.* **2001,** *67*, (9), 4024-4029.

70. Yang, Y.; Chen, B.; Hower, J.; Schindler, M.; Winkler, C.; Brandt, J.; Di Giulio, R.; Ge, J.; Liu, M.; Fu, Y.; Zhang, L.; Chen, Y.; Priya, S.; Hochella, M. F., Discovery and ramifications of incidental Magnéli phase generation and release from industrial coal-burning. *Nat. Commun.* **2017,** *8*, (1), 194.

71. Yuan, Y.; He, K.; Byles, B. W.; Liu, C.; Amine, K.; Lu, J.; Pomerantseva, E.; Shahbazian-Yassar, R., Deciphering the Atomic Patterns Leading to MnO2 Polymorphism. *Chem* **2019,** *5*, (7), 1793-1805.

72. Toyoda, K.; Tebo, B. M., Kinetics of Mn(II) oxidation by spores of the marine Bacillus sp. SG-1. *Geochim. Cosmochim. Acta* **2016,** *189*, 58-69.

73. Soldatova, A. V.; Balakrishnan, G.; Oyerinde, O. F.; Romano, C. A.; Tebo, B. M.; Spiro, T. G., Biogenic and Synthetic MnO2 Nanoparticles: Size and Growth Probed with Absorption and Raman Spectroscopies and Dynamic Light Scattering. *Environmental Science & Technology* **2019,** *53*, (8), 4185-4197.

74. Spiro, T. G.; Bargar, J. R.; Sposito, G.; Tebo, B. M., Bacteriogenic manganese oxides. *Acc. Chem. Res.* **2009,** *43*, (1), 2-9.

75. Lee, S.; Xu, H., XRD and TEM studies on nanophase manganese oxides in freshwater ferromanganese nodules from Green Bay, Lake Michigan. *Clays and Clay Minerals* **2016,** *64*, (5), 523-536.

76. Webb, S.; Tebo, B.; Bargar, J., Structural characterization of biogenic Mn oxides produced in seawater by the marine Bacillus sp. strain SG-1. *Am. Mineral.* **2005,** *90*, (8-9), 1342-1357.

77. Santelli, C. M.; Webb, S. M.; Dohnalkova, A. C.; Hansel, C. M., Diversity of Mn oxides produced by Mn (II)-oxidizing fungi. *Geochim. Cosmochim. Acta* **2011,** *75*, (10), 2762-2776.

78. Webb, S.; Fuller, C.; Tebo, B.; Bargar, J., Determination of uranyl incorporation into biogenic manganese oxides using X-ray absorption spectroscopy and scattering. *Environ. Sci. Technol.* **2006,** *40*, (3), 771-777.

79. Feng, X. H.; Tan, W. F.; Liu, F.; Wang, J. B.; Ruan, H. D., Synthesis of todorokite at atmospheric pressure. *Chem. Mater.* **2004,** *16*, (22), 4330-4336.

80. Atkins, A. L.; Shaw, S.; Peacock, C. L., Nucleation and growth of todorokite from birnessite: Implications for trace-metal cycling in marine sediments. *Geochim. Cosmochim. Acta* **2014,** *144*, 109-125.

81. Hu, X.; Kitchaev, D. A.; Wu, L.; Zhang, B.; Meng, Q.; Poyraz, A. S.; Marschilok, A. C.; Takeuchi, E. S.; Takeuchi, K. J.; Ceder, G.; Zhu, Y., Revealing and Rationalizing the Rich Polytypism of Todorokite MnO2. *J. Am. Chem. Soc.* **2018,** *140*, (22), 6961-6968.

669 82. Ilton, E. S.; Post, J. E.; Heaney, P. J.; Ling, F. T.; Kerisit, S. N., XPS Determination of Mn
670 Oxidation States in Mn (Hydr) oxides. *Appl. Surf. Sci.* **2016,** *366*, 475-485.
671 83. McMahon, P. B.; Belitz, K.; Reddy, J. E.; Johnson, T. D., Elevated Manganese
672 Concentrations in United States Groundwater, Role of Land Surface–Soil–Aquifer Connections.
673 *Environ. Sci. Technol.* **2019,** *53*, (1), 29-38.
674 84. Manning, B. A.; Fendorf, S. E.; Bostick, B.; Suarez, D. L., Arsenic (III) oxidation and
675 arsenic (V) adsorption reactions on synthetic birnessite. *Environ. Sci. Technol.* **2002,** *36*, (5), 976-
676 981.
677 85. Villalobos, M.; Escobar-Quiroz, I. N.; Salazar-Camacho, C., The influence of particle size
678 and structure on the sorption and oxidation behavior of birnessite: I. Adsorption of As(V) and
679 oxidation of As(III). *Geochim. Cosmochim. Acta* **2014,** *125*, 564-581.
680 86. Tang, Y.; Webb, S. M.; Estes, E. R.; Hansel, C. M., Chromium(iii) oxidation by biogenic
681 manganese oxides with varying structural ripening. *Environ. Sci.: Process. Impacts* **2014,** *16*, (9),
682 2127-2136.
683 87. Landrot, G.; Ginder-Vogel, M.; Livi, K.; Fitts, J. P.; Sparks, D. L., Chromium (III)
684 oxidation by three poorly-crystalline manganese (IV) oxides. 1. Chromium (III)-oxidizing capacity.
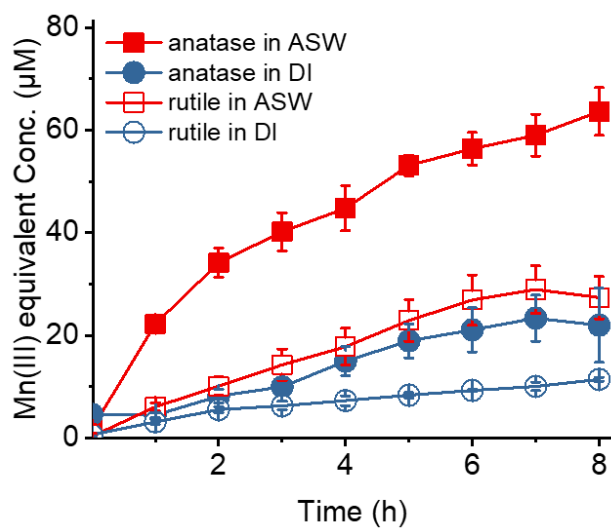685 *Environ. Sci. Technol.* **2012,** *46*, (21), 11594-11600.

686

687

688

Figure 1. Rapid photocatalytic oxidation of Mn^{2+}(aq) by anatase and rutile in artificial seawater (ASW) and deionized (DI) water.
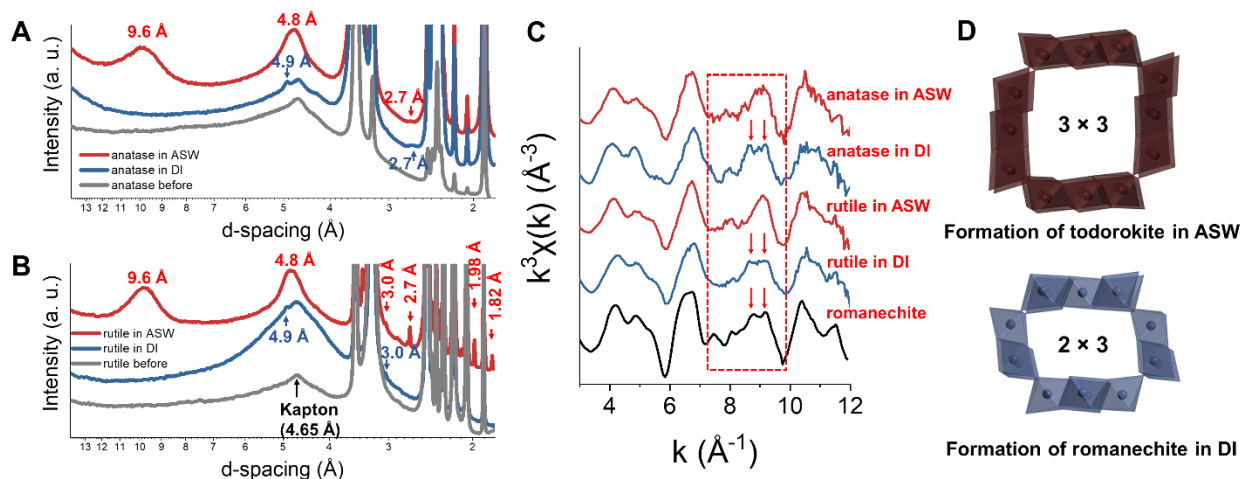
691

Figure 2. Formation of large tunnel structured Mn oxides on the surface of TiO_2. (A and B) Synchrotron XRD analyses show that the nucleated Mn oxide on the surface of both anatase and rutile in ASW is todorokite (3×3 tunnel structure). In DI system, weak diffraction occurred at 4.9 Å. Because several tunnel structured Mn oxides (romanechite (2×3), hollandite (2×2), and todorokite (3×3)) have diffraction peak at this position, it is challenging to identify the phase of Mn oxide using SXRD alone. (C) EXAFS analysis confirms that Mn oxides formed in DI system are structurally similar to romanechite. (D) Schematic structures of todorokite (3×3 tunnel size) and romanechite (2×3 tunnel size).
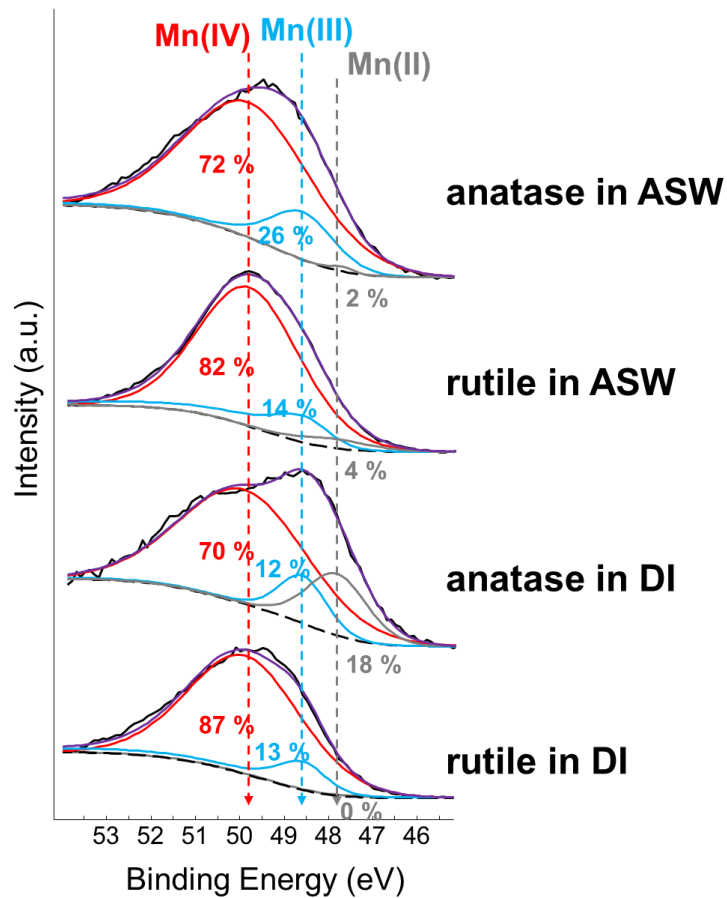
Figure 3. Mn 3p XPS spectra of Mn oxides formed on the surface of TiO_2. Fitting results show that all the Mn oxides formed under varied conditions have Mn(III). Mn oxides formed in the presence of anatase have more Mn(III) than those formed in the rutile system.
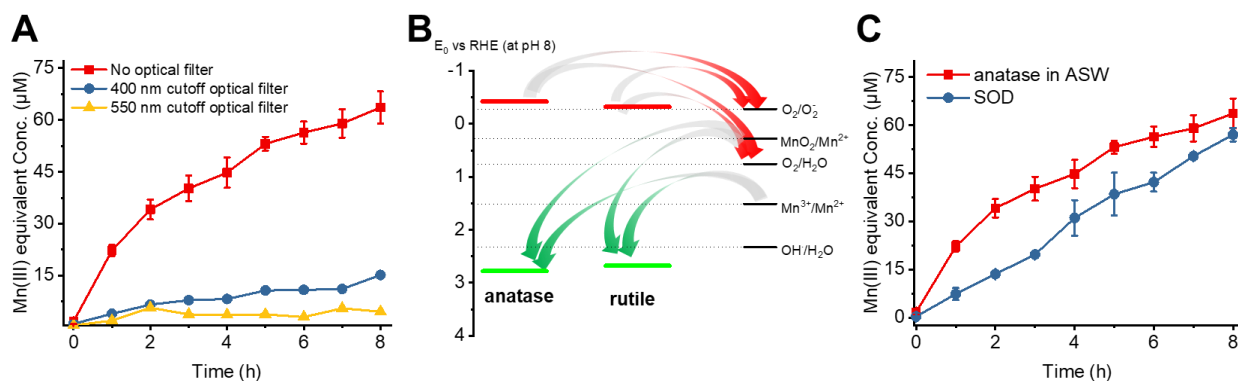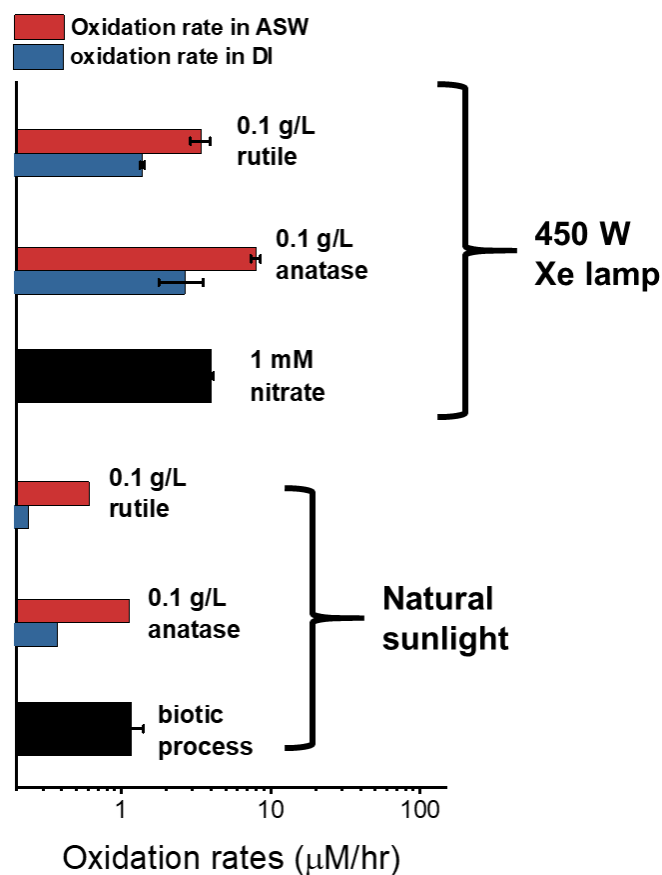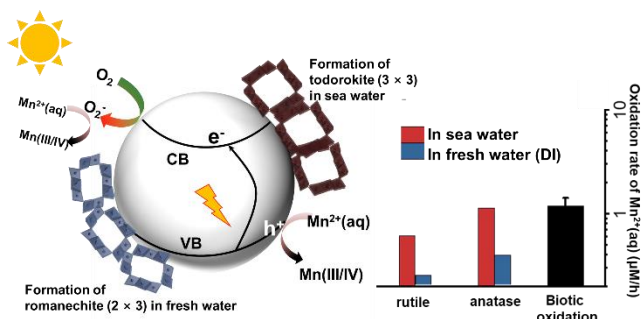
Figure 4. Mechanistic understanding of the photocatalytic oxidation of $Mn^{2+}(aq)$ in the presence of TiO_2. (A) Control tests with 400 or 550 nm optical cut off filters suggest that the rapid photocatalytic oxidation of $Mn^{2+}(aq)$ with TiO_2 occurs from the photo-excited electron-hole pair mainly at wavelength < 400 nm. (B) The positions of valence and conduction bands show that the photocatalytic oxidation of $Mn^{2+}(aq)$ with TiO_2 is thermodynamically feasible via both direct electron transfer and indirect reaction of $Mn^{2+}(aq)$ with photocatalytically generated superoxide. (C) The decrease of oxidation rate in the presence of superoxide dismutase (SOD; a superoxide scavenger) indicates that both superoxide and photo-excited holes contribute to the rapid oxidation of $Mn^{2+}(aq)$ in the presence of TiO_2 and light. In addition, the occurrence of superoxide indicates that oxygen is the electron acceptor, which enables the rapid direct electron transfer from $Mn^{2+}(aq)$ to a hole in the valence band of TiO_2 by blocking the recombination of electron-hole pair.

Figure 5. Comparison of the photocatalytic oxidation rates of Mn^{2+}(aq) in this study (using Xe lamp or calculated to natural sunlight condition) with previously reported oxidation rates in the presence of nitrate or via biotic processes.

717

718

719

720

721

722   **TOC graphic**